Volume 4
Number 8
August 2025
Pages 1133–1336

Environmental Science Advances

rsc.li/esadvances

ISSN 2754-7000

ROYAL SOCIETY OF CHEMISTRY

PAPER

Chandan Tamuly *et al.*

Optimized colorimetric detection of chromium ions (Cr^{3+}) using black garlic-Ag nanoparticles

Environmental Science Advances

ROYAL SOCIETY OF CHEMISTRY

PAPER

View Article Online
View Journal | View Issue

Check for updates

Cite this: *Environ. Sci.: Adv.*, 2025, **4**, 1211

Optimized colorimetric detection of chromium ions (Cr^{3+}) using black garlic-Ag nanoparticles†

Rintumoni Paw,[abc] Kangkan Sarmah,[d] Ankur K. Guha[d] and Chandan Tamuly*[ab]

Received 14th April 2025
Accepted 1st June 2025

DOI: 10.1039/d5va00100e

rsc.li/esadvances

In this study, AgNPs were synthesized using black garlic (BG) extract and applied for precise and sensitive colorimetric detection of chromium (Cr^{3+}) ions in solution. The nanoparticles (BG-AgNPs) were characterised using UV-visible spectroscopy, FTIR, SEM, TEM and XPS analysis. The UV-visible absorbance peak appeared at 411 nm. The pattern of X-ray diffraction (XRD) confirmed a face-centered cubic (FCC) structure of the AgNPs. The SEM images displayed a fusiform (spindle-shaped) morphology of the AgNPs. Transmission electron microscopy (TEM) images presented the sphere-shaped nature of the nanoparticles having a mean diameter of 16.02 ± 1.75 nm. The addition of Cr^{3+} ions turned the brownish BG-AgNP solution colourless. The sensor displayed a linear response to Cr^{3+} concentrations between 2 nM and 20 nM, with a limit of detection (LoD) of 0.07 nM. Optimal sensor performance was achieved at pH 7 and a temperature of 45 °C. Selectivity tests confirmed minimal interference from other metal ions. These results indicate that the developed nanosensor is exceptionally efficient and ultrasensitive at precisely detecting low concentrations of Cr^{3+} ions in environmental applications. A computational study with one of the most abundant compounds during the early stages of the aging process of black garlic formation, γ-glutamyl-S-allylmercaptocysteine (GSAMC), showed a binding energy of -6.67 kcal mol^{-1} for the formation of GSAMC-AgNPs and -8.82 kcal mol^{-1} for the formation of the GSAMC-AgNP-Cr complex.

Environmental significance

This study is highly significant from an environmental point of view. Chromium is a major pollutant in different industries affecting soil and water. Therefore, method development for the detection of Cr^{3+} ions at the nM level has significant importance for health, hygiene and human life.

Introduction

Chromium is highly valued for its shiny appearance and resistance to corrosion, making it a key material in industries such as steel production, electroplating, tanning, and chemical processing.[1] However, its widespread industrial use has contributed to environmental contamination. Both trivalent and hexavalent forms of chromium are used in various sectors, such as fossil fuel processing, metallurgy, leather treatment, dye production, metal fabrication, cement manufacturing, munitions, and timber preservation.[2–5]

Cr^{3+} is an essential trace nutrient necessary for human health.[6] Hexavalent chromium (Cr^{6+}) is reported to be highly carcinogenic, while the toxicological mechanisms of trivalent chromium (Cr^{3+}) are not well understood, leading to its classification as a category-III carcinogen.[7–9] Cr^{3+} can induce a wide range of responses in aquatic and terrestrial plants, including inhibited growth and seed germination, chloroplast damage, reduced photosynthesis, oxidative stress, and alterations in nutrient balance, organelle function, and cellular processes.[10]

Moreover, growing evidence suggests that Cr^{3+} is embryotoxic, with exposure during the preimplantation stage causing significant developmental issues in the *in vitro* fertile (IVF) mouse embryos, including growth arrest, reduced blastocyst formation, and increased cellular damage, even at low concentrations.[11]

Non-occupational exposure to chromium mainly comes from consuming contaminated food and drinking water, as well as from exposure to tobacco products that release chromium during pyrolysis.[12–15] Therefore, the detection of Cr^{3+} ions in drinking water is essential for safeguarding human health.

---

[a] *Natural Product Chemistry Section, CSIR-North East Institute of Science and Technology, Branch Itanagar, Arunachal Pradesh-791110, India. E-mail: c.tamuly@gmail.com*

[b] *Academy of Scientific and Innovative Research (AcSIR), Ghaziabad-201002, India*

[c] *Dept of Chemistry, Silapathar Science College, Silapathar, Assam-787059, India*

[d] *Dept of Chemistry, Cotton University, Guwahati, Assam-781001, India*

† Electronic supplementary information (ESI) available. See DOI: https://doi.org/10.1039/d5va00100e

Various qualitative and quantitative analytical methods exist for determining Cr^{3+}. Conventional methods encompass spectrometric techniques based on atomic absorption, atomic emission, and mass detection, along with other approaches such as X-ray fluorescence and voltammetry.[16–20] While these methods are highly accurate and sensitive, they have limitations, such as time-consuming sample preparation, high costs, the need for trained personnel to operate the instruments, and unsuitability for on-site applications.[21]

Colorimetric sensors are a simple, low-cost method for detecting Cr^{3+} as they do not require sophisticated instruments and can be easily visualized by the naked eye.[22–26] Silver nanoparticles (AgNPs) have been extensively used as colorimetric sensors for detecting various analytes, including metal ions, pesticides, and DNA, due to their surface plasmon resonance (SPR) absorption properties, which are highly sensitive to the shape, size, and surrounding chemical environment.[27–33] The mechanism behind AgNP-based colorimetric sensors involves a visible colour change from yellow to other colours, triggered by analyte-induced aggregation of AgNPs, leading to interparticle plasmon coupling.[34]

Various nanosensors have been developed to detect Cr^{3+}. These include AuNPs functionalized with polyethyleneimine, 4-mercaptobenzoic acid, 4-amino hippuric acid, 4-nitrobenzene mercaptan, citrate, and gallic acid, as well as Ag@mannose and AuNPs modified with 5,5′-dithiobis(2-nitrobenzoic acid). Ag@mannose nanoparticles detect Cr^{3+} ions *via* colour changes induced by nanoparticle aggregation involving surface-bound mannose. Cr^{3+} detection has also been demonstrated using AuNPs modified with 5,5′-dithiobis(2-nitrobenzoic acid), achieving a detection limit of 25 ppb at pH 6. Additionally, colorimetric detection of Cr^{3+} in aqueous solutions has been reported using citrate-capped AgNPs. Another approach involves using AuNPs functionalized with 4-mercaptobenzoic acid for Cr^{3+} detection.[35]

AuNPs have also been designed using 4-mercaptobenzoic acid, polyethyleneimine, and 4-nitrobenzene mercaptan.[36,37] Among these, 4-MBA and PEI co-functionalized AuNPs demonstrated superior sensitivity, allowing for visual Cr^{3+} detection and analysis *via* UV-vis absorption spectroscopy, with a detection limit of 1 μM.[36]

In addition, colorimetric detection of Cr^{3+} has been demonstrated using AuNPs functionalized with 4-amino hippuric acid.[38] Elavarasi *et al.* designed a colorimetric assay and visual colour change method on paper to detect Cr^{3+} in aqueous solutions using citrate-capped AuNPs.[39] This approach relied on the clustering of citrate-functionalized AuNPs triggered by Cr^{3+} ions. This clustering resulted in a redshift of the colorimetric absorption peak from 526 nm to 714 nm. Furthermore, a selective colorimetric assay for detecting both Cr^{3+} and Cr^{6+} using gallic acid-capped AuNPs has also been reported, where colour changes are induced by nanoparticle aggregation.[40]

The objective of this study is to develop a colorimetric technique for detecting Cr^{3+} ions, utilizing AgNPs synthesized using black garlic (BG) extract. Black garlic is a health-promoting ingredient that is widely available in international markets. It is produced by roasting fresh garlic (*Allium sativum L.*) under controlled conditions involving high temperature and humidity over an extended period. This process darkens the garlic cloves, enhances their sweetness, and transforms their texture into a chewy, jelly-like consistency. The fermentation duration varies based on cultural practices, manufacturers, and intended purposes.[41] It is well known that the aging period is shorter at higher temperatures.[42] For example, at 70 °C, the aging process is twice as fast compared to 60 °C.[43] During aging, the cloves turn dark brown and develop a sweet, tangy taste as the pungent odour diminishes.[44] Significant chemical changes occur during heating, primarily through the Maillard reaction, which involves the condensation of amino groups with reducing sugars.[45,46] Organosulfur compounds are key components in garlic. Eight major compounds identified in black garlic are diallyl disulfide, allicin, ajoene, S-allyl-mercapto-L-cysteine, S-allyl-L-cysteine, S-(propenyl)-L-cysteine, γ-glutamyl-S-allylcysteine, and γ-glutamyl-S-(1-propenyl)-L-cysteine.[47–50] Additionally, γ-glutamyl-S-allylmercaptocysteine (GSAMC) is predominantly formed during the early stages of aging. It is derived from γ-glutamyl-S-allylcysteine or γ-glutamyl-S-1-propenyl-L-cysteine, with its concentration peaking at around one month before declining as aging continues.[51–55]

Materials and methods

Materials

Forty-day fermented peeled black garlic was procured from Aasward Implex LLP, Vadodara, India. Analytical grade $ZnSO_4 \cdot 7H_2O$ (99.99%), $CrCl_3$ (99.9%), $MgCl_2 \cdot 6H_2O$ (99.99%), $PdCl_2$ (99%), $NiCl_2$ (98%), $CoCl_2$, $MnCl_2 \cdot 2H_2O$, $Pb(NO_3)_2$, $AlCl_3$, $BaCl_2 \cdot 2H_2O$ (99%), and $CaCO_3$ (99%) were purchased from Sigma-Aldrich.

Preparation of BG-AgNPs

Four cloves of black garlic were ground using a mortar and pestle, and 200 mL of H_2O was added to it. The mixer was then boiled for 15 min. Once cooled, the solution was passed through a microporous cellulose filter with a 20–25 μm pore size to collect the garlic extract (filtrate). The filtrate was kept at 4 °C for later use. A mixture was prepared by adding 10 mL of 1 mM $AgNO_3$ solution to 1 mL of the black garlic extract, followed by

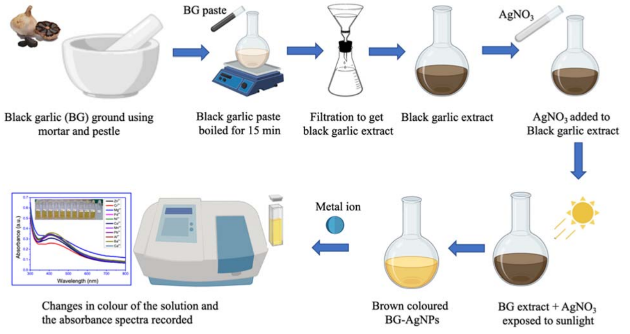

Fig. 1 Diagrammatic overview of BG-AgNP synthesis and the evaluation of their metal ion sensitivity.

exposing it to sunlight for 15 min. The colour changed to brown and the UV peak was observed at 411 nm (Fig. 1).[56]

Characterization of the synthesized AgNPs

The synthesized nanoparticles were characterized using a range of advanced techniques. UV-visible absorbance spectra were studied to confirm the synthesis of AgNPs and to analyze their plasmonic behaviour. Light beams from 300 to 800 nm wavelength were used for this purpose (UV-2600 spectrometer, Shimadzu Corp., Japan). Powder X-ray diffraction analysis using a source of Cu Kα radiation ($\lambda = 1.5406$ Å) was performed at a scanning speed of 3° per min (Bruker D8 Advance powder XRD, Germany) to characterize the crystalline nature. Transmission electron microscopy (TEM) images were acquired using an accelerating voltage of 200 kV (JEM-2100 microscope, JEOL Ltd, Japan). Nanoparticle size, interplanar spacing, and *d*-spacing values were determined through a selected area electron diffraction (SAED) study and analysis using the software ImageJ. A field emission scanning electron microscope (Sigma 300 VP FE-SEM, ZEISS, Germany) operated at 15 kV accelerating voltage was used to obtain the surface morphology image of the nanoparticles. An X-ray photoelectron spectrometer (ESCALAB Xi + XPS, Thermo Fisher Scientific Inc., USA) was used to characterize the elemental composition, empirical formula, and electronic states of the constituent elements. Energy dispersive X-ray spectroscopy (EDX) based elemental composition of the nanoparticles was analyzed using an Aztec (Oxford Instruments, UK). The FTIR spectra were recorded using a Spectrum Two, PerkinElmer Inc., USA.

Selectivity as a metal ion sensor

To evaluate the metal ion selectivity of the synthesized BG-AgNPs, 1 mM solutions of the metal ions Zn^{2+}, Cr^{3+}, Mg^{2+}, Pd^{2+}, Ni^{2+}, Co^{2+}, Mn^{2+}, Pb^{2+}, Al^{3+}, Ba^{2+}, and Ca^{2+} were prepared in deionized water. A 0.2 mL aliquot of each 1 mM metal ion solution was added to 5 mL of a diluted BG-AgNP solution. The resulting mixture was vortexed for 2 min at room temperature to facilitate possible interactions. The chromogenic changes in the solutions were visually observed, and the spectrophotometric absorbance corresponding to the mixtures was measured in the wavelength range from 300 nm to 800 nm. Variations in peak positions were analyzed to determine the interactions with the metal ions and to evaluate the specificity of the nanoparticles.

Optimization of detection parameters

The peak absorbance of 5 mL BG-AgNPs was measured at room temperature after adding 10 μL of 0.01 mM Cr^{3+} across different pH levels: 1, 4, 7, 9, and 12 to optimize the pH. For optimization of temperature, the peak absorbance of 5 mL BG-AgNP solution was measured after adding 10 μL of 0.01 mM Cr^{3+} at pH 7, across a temperature range of 35–95 °C, at an interval of 10 °C. The study examined the impact of temperature and pH on the sensitivity of BG-AgNPs for Cr^{3+} by calculating the relative activity. The relative activities were calculated from the absorbance peak using the following formula (eqn (1)):[57]

$$\text{Relative activity (\%)} = [(M_2 - M_1)/M_2] \times 100 \tag{1}$$

where M_1 is the peak absorbance of the BG-AgNP-Cr^{3+} mixture under the experimental conditions, and M_2 is the highest peak absorbance of the BG-AgNP-Cr^{3+} mixture in the experiment.

Limit estimation for sensing Cr^{3+} ions

Initially, 10–100 μL from 0.01 mM solution of Cr^{3+} (2–20 nM) was added to 5 mL of BG-AgNPs, and their absorbance was measured at a wavelength of 411 nm. To determine the lowest detectable quantity of Cr^{3+}, a linear calibration curve was plotted using the formula (eqn (2)):

$$Y = a + bX, \tag{2}$$

where Y represents the peak absorbance, X denotes the quantity of Cr^{3+}, b is the slope, a is the Y-intercept, and b represents the linear calibration slope.

The limit of detection and quantification (LoD and LoQ) were determined using eqn (3) and (4):[58]

$$\text{LoD} = \frac{3.3 \times \text{SD}}{S} \tag{3}$$

$$\text{LoQ} = \frac{10 \times \text{SD}}{S} \tag{4}$$

where SD represents the standard deviation of the peak absorbance of 5 mL of BG-AgNPs without Cr^{3+} ($n = 5$), and S is the linear calibration slope.

Reaction kinetics between BG-AgNPs and Cr^{3+}

To explore the interaction kinetics between BG-AgNPs and Cr^{3+}, varying volumes (25, 50, and 75 μL) of a 0.01 mM Cr^{3+} solution were added to 5 mL of BG-AgNPs. The spectroscopic absorbance of the resulting mixtures was recorded at an interval of 5 min. The following linear kinetic models were evaluated in the current study (eqn (5)–(7)):[59]

$$\text{Zero order: } [A_t] = [A_0] - k_0 t \tag{5}$$

$$\text{First order: } \ln([A_t]/[A_0]) = -k_1 t \tag{6}$$

$$\text{Second order: } 1/[A_t] = k_2 t + 1/[A_0] \tag{7}$$

In these equations, $[A_t]$ represents the peak absorbance at time t, while $[A_0]$ is the peak absorbance at $t = 0$. The constants k_0, k_1 and k_2 correspond to the zero, first and second-order rate constants, respectively. The kinetic models are illustrated by plotting $[A_t]$ against T, $\ln([A_t]/[A_0])$ against T and $1/[A_t]$ against T, respectively. The constants k_0, k_1 and k_2 were determined from the slopes of the corresponding linear plots.

Interference study

To evaluate the potential interference of common ions, 0.2 mL of 1 mM solution of $CrCl_3$ was added to 3 mL of BG-AgNPs. Next, 0.2 mL of 1 mM salt solution ($ZnSO_4$, $MgCl_2$, $PdCl_2$, $NiCl_2$, $CoCl_2$, $MnCl_2$, $Pb(NO_3)_2$, $AlCl_3$, $BaCl_2$, and $CaCO_3$) was added individually to this mixture. The solutions were vortexed for 2 min to facilitate possible reactive interactions, and then the colorimetric absorbance spectra were recorded.[60]

Five replicate measurements were conducted for the control (containing only Cr^{3+}) and for each salt-added mixture. F-test (ANOVA) was performed using the software Origin 9 to determine whether the addition of other ions caused significant changes in absorbance.

Computational details

Density Functional Theory (DFT) was utilized to analyze the bonding interactions between Ag and the COOH group of the GSAMC molecules. The computations were performed using the M06-2X functional in conjunction with the def2-TZVP basis set,[61] within the Gaussian 16 software suite.[62] To understand the molecular orbital interactions, natural bond orbital (NBO) analysis was performed.[63]

To calculate the Gibbs free energy of the proposed reaction of $AgNO_3$ with GSAMC and the Cr complex of the GSAMC-Ag nanoparticles, we used the following equations (eqn (8) and (9)).

$$\Delta G_1 = [\{G_{\text{GSAMC-Ag-NPs}}\} - \{G_{\text{AgNO}_3} + G_{\text{GSAMC}}\}] \tag{8}$$

$$\Delta G_2 = [\{G_{\text{GSAMC-Ag-NP-Cr}}\} - \{G_{\text{GSAMC-Ag-NPs}} + G_{\text{Cr}}\}] \tag{9}$$

where $G_{\text{GSAMC-Ag-NPs}}$, G_{AgNO_3} and G_{GSAMC} are the Gibbs free energies of γ-glutamyl-S-allylmercaptocysteine (GSAMC)-silver nanoparticles, $AgNO_3$ and γ-glutamyl-S-allylmercaptocysteine molecules, respectively, for reaction 1. Similarly, $G_{\text{GSAMC-Ag-NP-Cr}}$ and G_{Cr} are the Gibbs free energy of the γ-glutamyl-S-allylmercaptocysteine (GSAMC)-silver chromium complex and the Cr^{3+} ion, respectively. All the structures were confirmed to be at their local minima, as indicated by the real values in the Hessian matrix.

Results and discussion

Characterization of the BG-AgNPs

Upon exposure to sunlight, the addition of black garlic extract into a colourless $AgNO_3$ solution induced the development of a yellowish-brown colouration within 15 minutes, signifying the synthesis of AgNPs. The reduction of silver ions (Ag^+) to metallic silver (Ag^0), leading to the synthesis of silver nanoparticles (AgNPs), was additionally confirmed through UV-visible spectroscopy, which displayed a characteristic SPR peak at 411 nm. This SPR peak confirms the successful formation of AgNPs (Fig. 2A).[56]

X-ray diffraction (XRD) analysis

The XRD data of the synthesized BG-AgNPs showed strong diffraction peaks at angles corresponding to 2θ values of 38.22°, 44.56°, 64.34°, and 78.20°. These peaks are associated with the (111), (200), (220), and (311) crystallographic planes, and are characteristic indicators of the typical face-centered cubic (FCC) lattice structure of silver (Fig. 2B). The XRD analysis is consistent with the reference data from the International Centre for Diffraction Data (ICDD), specifically PDF Card No. 00-004-0783.[64] The similarity in the peaks with the reference pattern confirms the crystalline nature of the BG-AgNPs.

Electron microscopy analysis (SEM and TEM)

The scanning electron micrograph (Fig. 3A) of BG-AgNPs revealed a fusiform (spindle-shaped) morphology of the

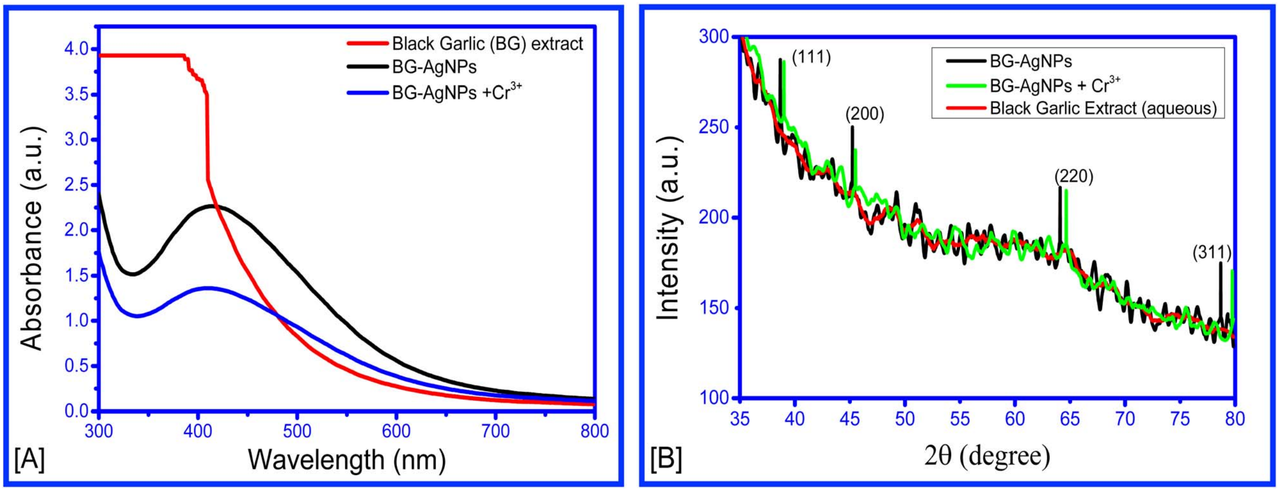

Fig. 2 (A) UV-vis spectra of black garlic extract, BG-AgNPs and BG-AgNPs + Cr^{3+} complex solution. (B) XRD crystallography of black garlic extract, BG-AgNPs and BG-AgNPs + Cr^{3+} complex.

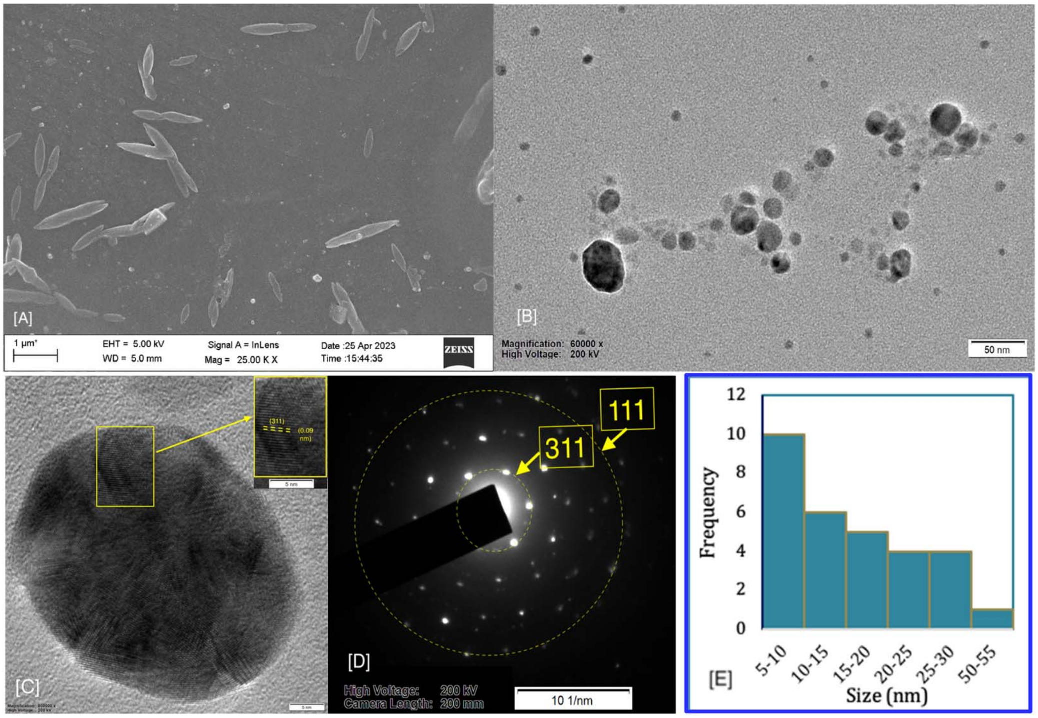

Fig. 3 (A) Scanning Electron Microscopy (SEM) image of black garlic-mediated silver nanoparticles (BG-AgNPs); (B and C) Transmission Electron Microscopy (TEM) (bright field) images illustrating the morphology of BG-AgNPs; (D) SAED pattern for a single BG-AgNP; (E) histogram depicting the size distribution of the nanoparticles, calculated using ImageJ software.

AgNPs, with a length of 0.85 ± 0.059 µm and a width of 0.22 ± 0.01 µm ($N = 29$) at the broadest point. Similar fusiform structures have been reported for CuO nanoparticles, Au nanoparticles, β-FeOOH, and α-Fe_2O_3 nanorods in other studies.[65,66]

Fig. 3B presents a transmission electron micrograph of the BG-AgNPs, confirming the spherical morphology of the nanoparticles. The nanoparticle diameter was 16.02 ± 1.75 nm (range 5.298 to 50.344 nm) ($N = 31$), as shown in Fig. 3E. Notably, nanoparticles in the 5–10 nm range were found to be the most prevalent. The SAED of the BG-AgNPs was indicative of the crystalline nature of the sample. The SAED analysis exhibited a face-centred cubic (FCC) crystal lattice with measured d-spacings of 3.21 ± 0.61 1/nm, 5.86 ± 0.53 1/nm, 9.22 ± 0.25 1/nm, and 12.45 ± 0.37 1/nm, associated with diffraction angles of 38.22°, 44.56°, 64.34°, and 78.20°, respectively (Fig. 3D). The interplanar distance calculated from the TEM measured 0.09 nm for the (311) plane at $2\theta = 78.20°$ (Fig. 3C).

X-ray photoelectron spectroscopy (XPS)

The XPS data revealed binding energy signals for S2p, C1s, Ag3d, N1s and O1s (Fig. 4). The S 2p peak is a doublet split into S $2p_{3/2}$ and S $2p_{1/2}$, with a typical spin–orbit splitting of ~1.2 eV. The S 2p binding energy at 167.7 eV and 168 eV suggests the presence of oxidized or covalently bonded sulfur species, and –S–S– (disulfide) is a likely assignment. It also indicates sulfur in one chemical state. This data envelope is fit to a spin–orbit doublet (the S $2p_{3/2}$ and $2p_{1/2}$ peaks) with the correct separation (1.2 eV).[67] The peaks for C1 are observed at 284.8 eV and 285.95 eV. A binding energy of 284.8 eV in the C1s XPS spectrum corresponds to C–C (sp^3 hybridized carbon) and C–H bonds, which are typically found around ~285 eV.[68] The detection of double peaks in the Ag 3d region suggests metallic silver (Ag^0) as the predominant constituent, with binding energies of 368.2 eV for Ag^0 $3d_{5/2}$ and 373.95 eV for Ag^0 $3d_{3/2}$, related to the AgNPs (Fig. 4B). Primary amine (–NH_2) has an N1s binding energy around ~399.5–400.5 eV. So, the binding energy peak observed at 399.9 eV indicated the presence of the –NH_2 group.[69] Binding energy peaks for O1s were observed at 532.45 eV and 532.55 eV in the O1s XPS spectrum, typically corresponding to –C–OH and –C=O.[70]

BG-AgNPs as selective Cr^{3+} nanosensors

The selectivity of BG-AgNPs was analyzed for the metal ions Zn^{2+}, Cr^{3+}, Mg^{2+}, Pd^{2+}, Ni^{2+}, Co^{2+}, Mn^{2+}, Pb^{2+}, Al^{3+}, Ba^{2+}, and Ca^{2+}. Among these, Cr^{3+} was the only metal ion that induced a significant change in the colour of the BG-AgNP solution, shifting from reddish-brownish to transparent. Cr^{3+} also significantly reduced the peak absorbance compared to other studied ions (Fig. 5A and S2†). The findings indicated that solutions of other ions were unable to significantly alter the plasmonic characteristics of the BG-AgNP solution (Fig. 5A and B). The LoD and LoQ were calculated to be 0.07 nM and 0.21 nM, respectively, using concentrations in the range of 2–20 nM. The slope of the regression line ($Y = 1.339–0.02481X$),

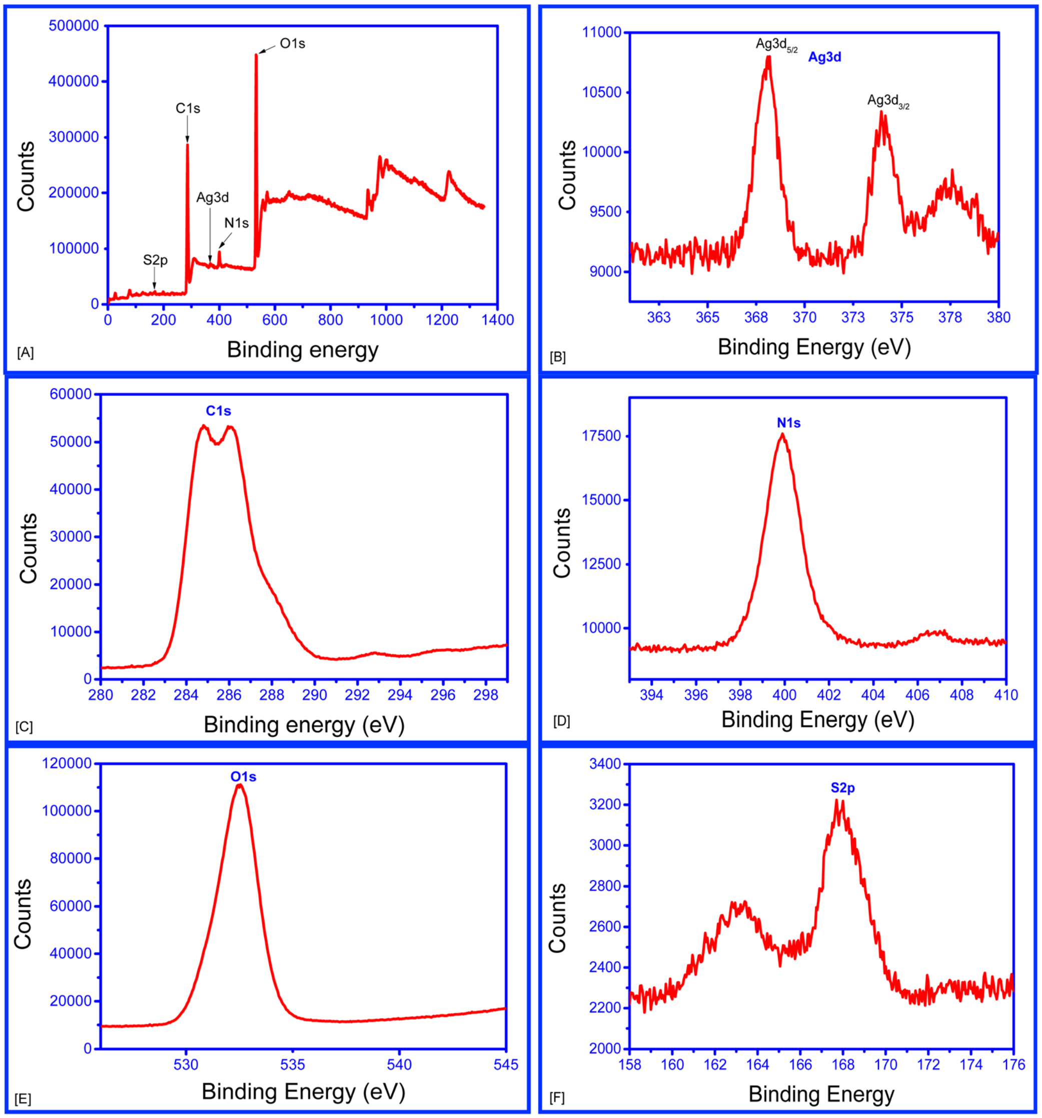

Fig. 4 (A) XPS survey scan of BG-AgNPs, (B) XPS Ag 3d scan, (C) XPS C1s scan (D) XPS N1s scan, (E) XPS O1s scan, and (F) XPS S2p scan.

which described the relationship between Cr^{3+} ion concentration and absorbance at 411 nm, was determined to be 0.02481. The Pearson correlation coefficient was $r = 0.988$, with an R^2 value of 0.97, indicating a strong linear correlation. The standard deviation of the absorbance at 411 nm, based on measurements from five samples, was 0.00053 (Fig. 5C and D). The change in colour and the absorbance may be due to the aggregation of the AgNPs resulting from AgNPs-Cr complex formation. Cr^{3+} induced aggregation in AgNPs and other metal nanoparticles has also been reported in previous studies (Table 1).[21,37–39,71]

Energy-dispersive X-ray spectrometry (EDX) was used to determine the chemical composition of the nanoparticle surface. As shown in Fig. S1† the nanoparticle surface contained C K (weight % 65.37, atomic % 71.84), O K (weight % 34.05, atomic % 28.09), and Ag L (weight% 0.59, atomic % 0.07), and after addition of Cr^{3+} ions, the chemical composition of the surface was C K (weight % 73.84%, atomic % 79.06), O K (weight % 26.01, atomic % 20.91), Cr K (weight % 0.08, atomic % 0.02), and Ag L (weight% 0.08, atomic % 0.01). The high percentage of C indicated the presence of organic molecule.[72] The oxygen at the material surface indicated the presence of functional groups.[73] A decrease in oxygen content after the addition of Cr^{3+} suggested possible interaction or reduction reactions occurring due to Cr^{3+} ions. The presence of chromium confirms that Cr^{3+} ions were successfully introduced to the nanoparticle surface. The minimal change in Ag content suggests that Ag is not significantly affected by Cr^{3+} addition. Though sulfur (S) was found in the XPS analysis, there was no visible S peak in the spectrum. The possibility may be that S was below the detection limit or sulfur may be embedded inside the nanoparticle, and it might not appear in the spectrum.

The FTIR spectra reveal key functional groups present in the samples before and after the addition of Cr^{3+} ions (Fig. S3†). A

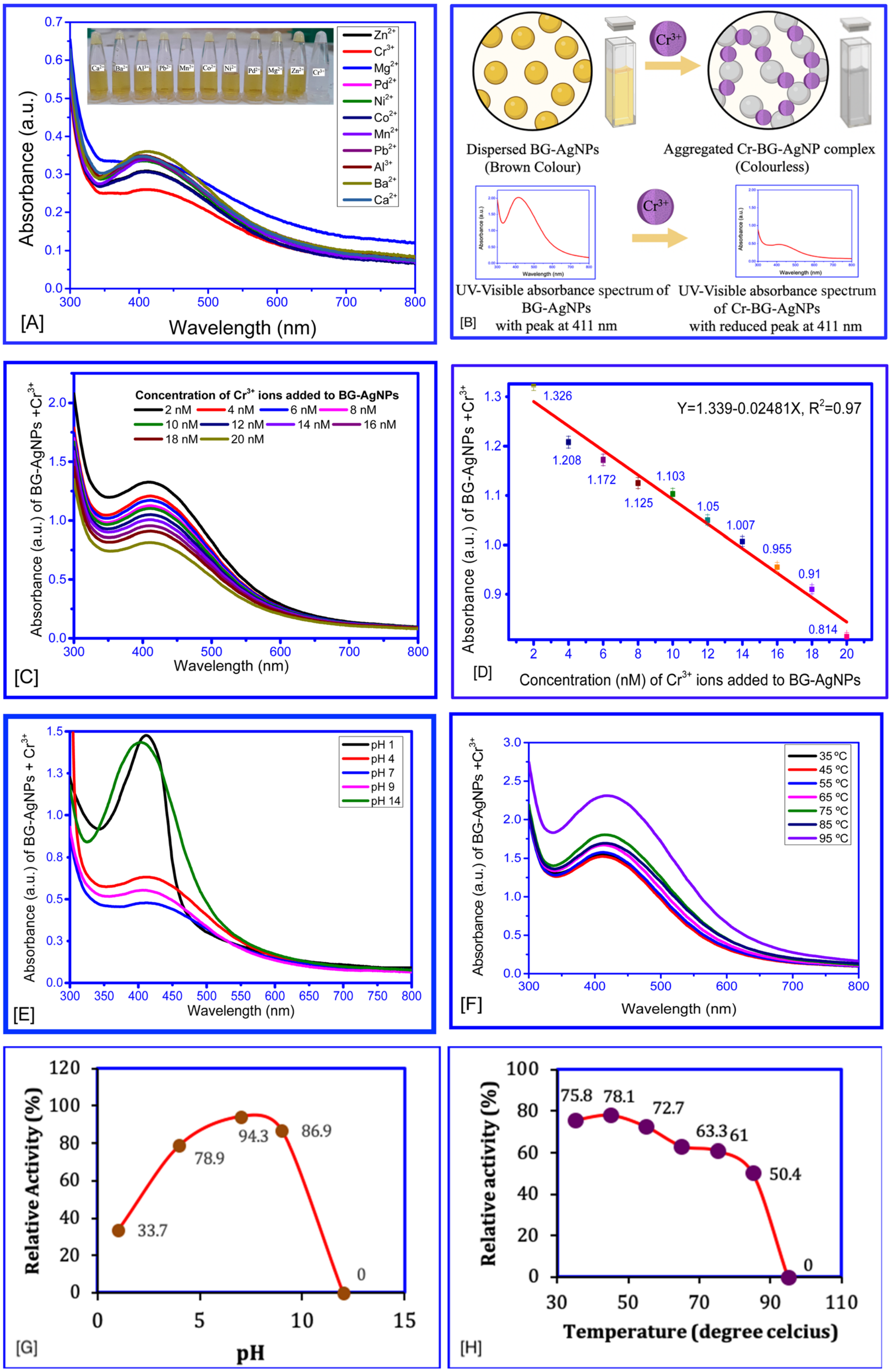

Fig. 5 (A) UV-visible spectra of BG-AgNPs following the addition of various metal ion solutions; (B) possible principle behind change in colour and UV-visible spectra of BG-AgNPs after adding Cr^{3+}, (C) UV-visible spectra of BG-AgNPs after adding Cr^{3+} solution, with concentrations ranging from 2 nM to 20 nM; (D) linear calibration plot of peak absorbance *versus* Cr^{3+} concentration; (E and F) UV-visible spectra of BG-AgNPs + Cr^{3+} ions measured at different pH levels and temperatures. (G and H) Relative activity of the BG-AgNPs in detection of Cr^{3+} at different pH and temperature.

Table 1 Comparison of the limit of detection (LoD) for Cr^{3+} analysis using the proposed BG-AgNP-based approach with those reported in previous studies

Sl. No.	Probe	Absorbance wavelength (nm)	Calibration range	LoD
1	Atomic absorption spectrometry[78]	—	—	0.577 μM
2	Fluorescence[79]	—	17–667 μM	1.7×10^4 μM
3	Hyper Rayleigh Scattering (HRS) using AuNPs functionalized with DNTB[80]	630	0–250 ppb	3.035 μM
4	Pyridoxal conjugated AuNPs assay[81]	625	7.5×10^{-5}–1.2×10^{-5} M	11.5 μM
5	Rhodamine capped AuNPs assay[82]	—	—	9.28 μM
6	EDTA- tannic acid-AgNPs[21]	429	2–5 mg L^{-1}	29.2 μM
7	Citrate-capped AuNPs[83]	520	0.2–1.0 ppm	0.98 μM
8	Citrate capped AuNPs[39]	526	10^{-3}–10^{-6} M	0.106 μM
9	5,5′-Dithiobis (2-nitrobenzoic acid) (DTNBA) AuNPs[84]	650/524	0–6 μM	1.8 μM
10	4-Amino hippuric acid (PAH)-AuNPs[38]	520	5 to 120 μM	1.17 μM
11	4- Mercaptobenzoic acid AuNPs[71]	635/520	20 to 25 μM	5 μM
12	4-Mercaptobenzoic acids (4-MBA)-Au@Ag NPs[37]	675/410	10 to 500 μM	9 μM
13	Meso-2,3-dimercaptosuccinic acid (DMSA)-Au NPs[85]	650/525	10–500 nM	10 nM
14	6- Mercaptonicotinic acid (MNA) and melamine (MA) functionalized Ag NPs[86]	535	10–370 μM	64.51 μM
15	**BG-AgNPs (present study)**	**411**	**2-20 nM**	**0.07 nM**

broad peak observed around 3276–3262 cm^{-1} corresponds to O–H stretching, likely from hydroxyl (–OH). A distinct peak at 1636 cm^{-1} revealed the presence of C=O stretching. The low frequency of carbonyl indicated the presence of amide carbonyl. A weak peak at 2156–2158 cm^{-1} may indicate the presence of unbound gaseous CO. The spectrum of AgNPs synthesized using black garlic extract showed the same functional groups as BG extract but confirmed the formation of nanoparticles through the retention of stabilizing biomolecules.[74]

The X-ray diffraction (XRD) analysis was performed on three different samples: black garlic extract, BG-AgNPs, and BG-AgNPs + Cr^{3+}, to examine their crystallinity and phase composition. The XRD patterns revealed significant differences between the samples, particularly regarding the formation of face-centred cubic (FCC) AgNPs. The XRD pattern of black garlic extract exhibited broad peaks with no distinct sharp diffraction signals, suggesting its amorphous nature. No FCC peaks corresponding to Ag were detected, confirming the absence of crystalline Ag phases. Like BG-AgNPs, the Cr^{3+}-BG-AgNP complex also showed strong diffraction peaks at angles corresponding to 2θ values of 38.22°, 44.56°, 64.34°, and 78.20°. These peaks are associated with the (111), (200), (220), and (311) crystallographic planes, and are characteristic indicators of the typical FCC lattice structure of Ag (Fig. 2B).[64]

Optimization of pH and temperature

The UV-visible absorbance spectra indicated that peak absorbance decreases in the presence of Cr^{3+} ions. Fig. 5E and G show that, when comparing UV absorbance at different pH levels, pH 7 exhibited the highest reduction in peak absorbance and the highest relative activity (94.3%). In case of temperature, the highest reduction in peak absorbance was observed at a temperature of 45 °C with the highest relative activity (Fig. 5F and H). These results suggested that pH 7 and 45 °C are the optimal conditions for detecting Cr^{3+} ions. Hamada *et al.*, in

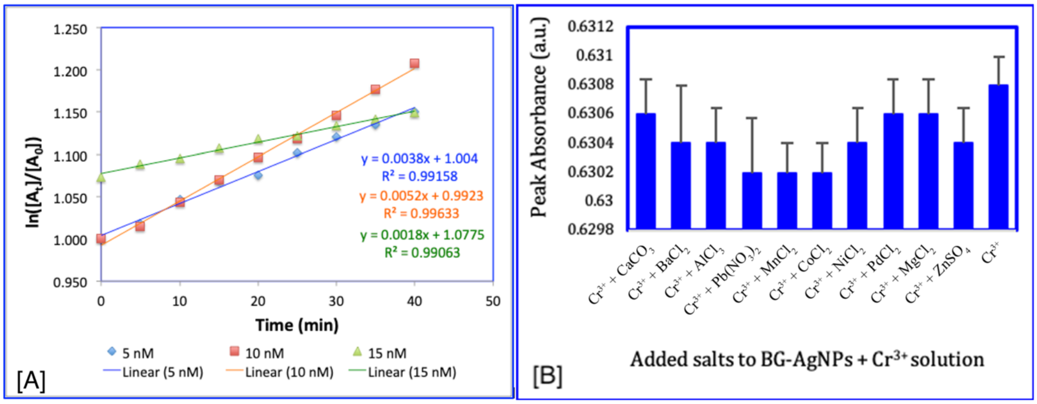

Fig. 6 (A) Changes in the peak absorbance of BG-Ag NPs over time in the presence of 5 nM, 10 nM and 15 nM Cr^{3+} at 5-min intervals, and the first order reaction kinetics model. (B) Interference study of different metal ions on the absorbance of the BG-AgNP-Cr^{3+} ion system.

a study of metal complex formation resulting from the reactions between Cr^{3+} and aspartic acid at different pH ranges, reported that the absorbance of the Cr^{3+}-aspartic acid system in a 1 : 2 ratio decreased as the pH increased from 1.55 to 4.10.[75] Present observation also aligns with the findings by Imai and Gloyna, who demonstrated that Cr^{3+} adsorption onto biological solids in activated sludge systems is maximized around neutral pH due to favourable ionic interactions and reduced competition from H^+ or OH^- ions.[76] However, the optimal conditions may vary with the nanoparticles as observed from the UV-vis spectra of 4-MBA-AuNP solutions in the presence of Cr^{3+}, which indicated pH 6 as its optimal condition over the range from 6 to 10.[71]

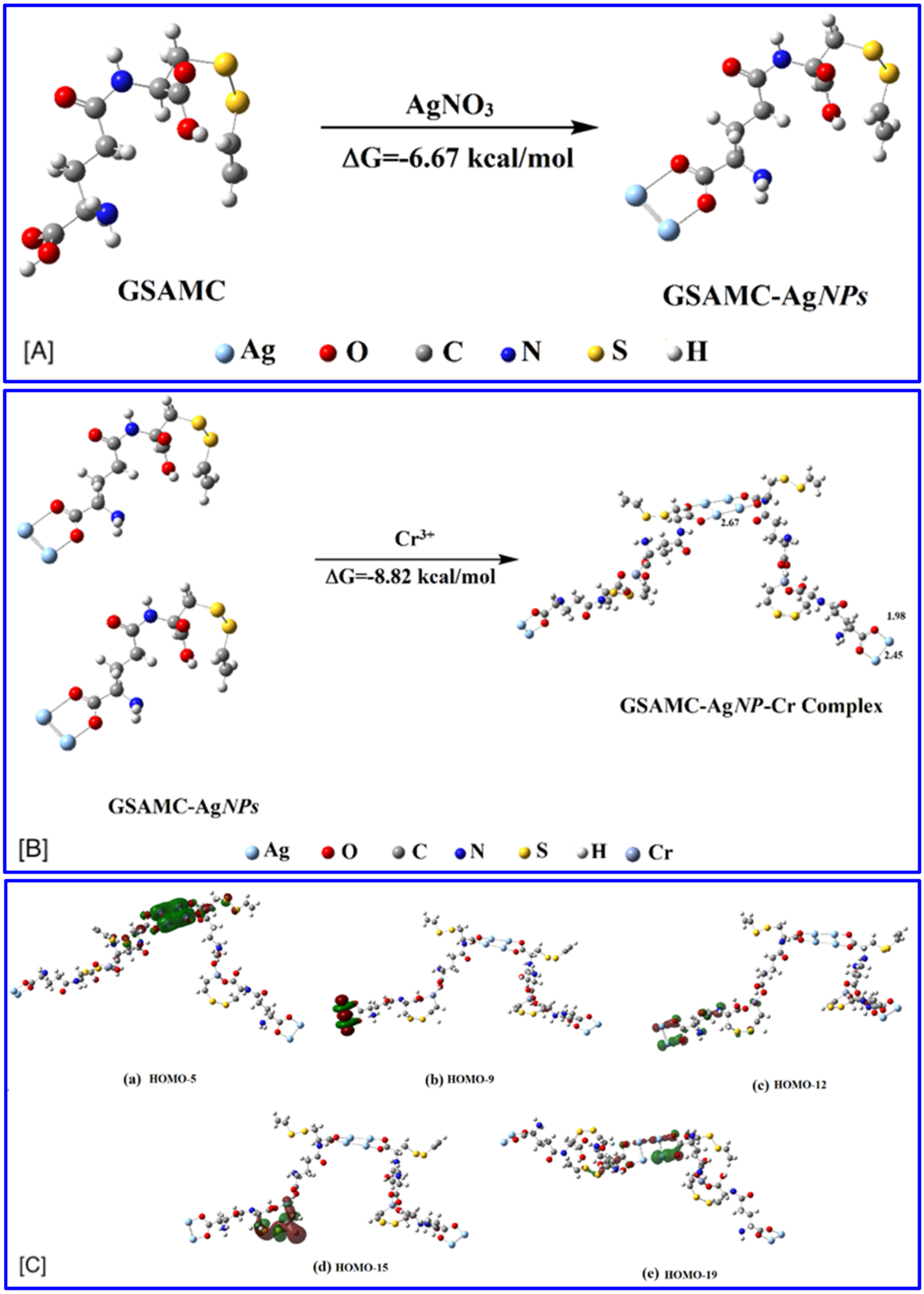

Fig. 7 (A) The reaction pathway of synthesized GSAMC-AgNPs. (B) The reaction pathways of the GSAMC-AgNP-Cr complex. Bond distances are in Å. (C) The molecular orbital diagram of Cr complexes of GSAMC-AgNPs.

The observation regarding temperature is strongly supported by Liu *et al.*, who reported that the adsorption of Cr^{3+} onto a spheroidal cellulose adsorbent was endothermic.[77] Their study showed that the adsorption capacity increased when the temperature was increased from 25 °C to 45 °C, highlighting a clear enhancement in Cr^{3+} binding.

Kinetics of the reactive interaction between BG-AgNPs and Cr^{3+}

To assess the kinetics of the binding between Cr^{3+} ions and BG-AgNPs, the change in absorbance over time was measured using UV-visible spectroscopy at different Cr^{3+} concentrations. UV-visible spectra were recorded every 5 min, showing a gradual decrease in absorbance of the Ag NPs in the presence of Cr^{3+} over time under uniform reaction conditions. This decline in absorbance was also associated with a decrease in the rate constant as the Cr^{3+} concentration decreased (Table S1†).

The investigation of the reaction dynamics between BG-AgNPs and Cr^{3+} demonstrated that a first-order kinetic framework provided the best fit for the data. It showed the highest R^2 coefficient when compared to zero and second-order models (Fig. 6A). Although two reactants, the nanoparticles and Cr^{3+} ions, are involved, the reaction followed pseudo-first-order kinetics. This behaviour indicated that the reaction rate primarily depends on the concentration of one reactant in the solution. The rate constants were determined to be 0.0038, 0.0052, and 0.0018 for Cr^{3+} concentrations of 25 μM, 50 μM, and 75 μM, respectively. These values were higher compared to those obtained for a second-order reaction (Table S1†).

Interference study

An F-test (ANOVA) indicated no statistical variation in the absorbance between the BG-AgNP + Cr^{3+} and the BG-AgNP + Cr^{3+} solutions with the addition of other ions ($F = 0.54$; $P = 0.85$; df = 10, 44). This suggests that the occurrence of these ions did not interfere with the detection of Cr^{3+} ions by the BG-AgNPs (Fig. 6B). The lack of interference can be attributed to the sensor's higher binding affinity for Cr^{3+} relative to other ions. The results of the selectivity assessment confirm that the BG-AgNP probe exhibited strong specificity to Cr^{3+} ions, with no significant impact from other commonly encountered ions. This high level of specificity is crucial for the accurate detection of Cr^{3+} in aquatic samples, enabling reliable and precise assessments.

Computational analysis

γ-Glutamyl-S-allylmercaptocysteine (GSAMC) is a compound derived from aged garlic extract. It primarily develops from GSAC/GS1PC during the initial stages of aging, attaining its maximum concentration around one month before diminishing in the later phases of the aging process.[55] Based on previous literature, it is hypothesized that GSAMC might be the bioactive compound responsible for the formation of BG-AgNPs and the detection of Cr^{3+}. To investigate this hypothesis, a computational study was conducted with GSAMC as the active compound.

The geometries of γ-glutamyl-S-allylmercaptocysteine (GSAMC) and Ag containing nanoparticles are optimized with the help of MO6-2X functional in combination with the def2-TZVP basis set.[61] The synthesis pathways of γ-glutamyl-S-allylmercaptocysteine (GSAMC)-silver nanoparticles (AgNPs) are illustrated in Fig. 7A, accompanied by the calculated Gibbs free energy values. The negative Gibbs free energy indicated that the reaction is thermodynamically favourable. After the study of the AgNP synthesis reaction, Fig. 7B depicts the synthesis pathways of the Cr containing γ-glutamyl-S-allylmercaptocysteine (GSAMC)-Ag complexes. Here also the Gibbs free energy is negative, indicating the thermodynamically favourable chemical reaction. All the structures shown in Fig. 7A and B are optimized.

In this synthesized GSAMC-AgNPs, the Ag atom interacts with the carboxylate group of the GSAMC molecule and the distance between the oxygen atom and Ag atom is 1.98 Å. The various types of bonding are described with the help of the molecular orbital analysis. In Fig. 7C(a), the Ag–Ag bond (HOMO-5) is shown, with a bond distance of 2.67 Å. The Ag atom linked with the carboxylate group is described by the help of molecular orbitals in Fig. 7C(b and c). After the addition of Cr, it linked with carboxylate and CH_2 groups of the S–S branch of GSAMC-AgNPs, and it is shown with help of the molecular orbital (HOMO-15) in Fig. 7C(d), The orbital in Fig. 7C(e) also represented the linkage of the oxygen atom and Ag in Cr complexes of GSAMC-AgNPs.

The molecular orbital analysis and Gibbs free energy analysis showed that the Ag-containing GSAMC formation is a feasible reaction, and after the addition of Cr, it forms a stable GSAMC-AgNP-Cr complex.

Conclusion

The advantages of the proposed colorimetric sensing approach are manifold. It offers a simple and cost-effective method that does not require sophisticated instrumentation, making it suitable for on-site environmental monitoring and resource-limited settings. Additionally, the BG-AgNPs demonstrate remarkable sensitivity in detecting Cr^{3+} ions at extremely low concentrations. Moreover, BG-AgNPs offer high selectivity, as they can discriminate Cr^{3+} ions from other metal ions commonly present in environmental samples.

Data availability

The data supporting this article have been included as part of the ESI.†

Author contributions

RP: conceptualization, investigation, analysis, manuscript preparation. KS & AKG: validation, software. CT: conceptualization, methodology, supervision, visualization, writing – review & editing. All read and approved the final version of the manuscript.

Conflicts of interest

The authors have no conflicts to declare.

Acknowledgements

The authors express their sincere appreciation to the Director, CSIR-North East Institute of Science and Technology, Jorhat, Assam, for the continuous support and valuable suggestions provided throughout the research (Manuscript ref: CSIR-NEIST/PUB/2024/099). The author thanks the Analytical Chemistry Group & SAIF, CSIR-NEIST, Jorhat, for their instrumental support. The authors thank the SEED Division, DST New Delhi (DST/SEED/TSP/STI/2022/915) for financial support.

References

1 P. J. Cunat, *Alloying Elements in Stainless Steel and Other Chromium-Containing Alloys*, Euro Inox, 2004.

2 P. B. Tchounwou, C. G. Yedjou, A. K. Patlolla and D. J. Sutton, Heavy metal toxicity and the environment, in *Molecular, Clinical and Environmental Toxicology, Experientia Supplementum*, ed. A. Luch, Springer, Basel, 2012, vol 101, pp. 133–164.

3 R. Chakraborty, K. Renu, M. A. Eladl, M. El-Sherbiny, D. M. A. Elsherbini, A. K. Mirza, B. Vellingiri, M. Iyer, A. Dey and A. V. Gopalakrishnan, *Biomed. Pharmacother.*, 2022, **151**, 113–119.

4 J. P. Wise, J. L. Young, J. Cai and L. Cai, *Environ. Int.*, 2022, **158**, 106877.

5 D. Y. Shin, S. M. Lee, Y. Jang, J. Lee, C. M. Lee, E. M. Cho and Y. R. Seo, *Int. J. Mol. Sci.*, 2023, **24**, 3410.

6 V. Gómez and M. P. Callao, *Trends Anal. Chem.*, 2006, **25**, 1006–1015.

7 G. M. Keegan, I. D. Learmonth and C. Case, *Crit. Rev. Toxicol.*, 2008, **38**, 645–674.

8 D. Beyersmann and A. Hartwig, *Arch. Toxicol.*, 2008, **82**, 493–512.

9 ATSDR, *Toxicological Profile for Chromium*, Public Health Service U.S. Department of Health and Human Services, Agency for Toxic Substances and Disease Registry, Atlanta, Georgia, 2012.

10 E. Salles, V. Normant and D. A. L. Vignati, A critical evaluation of chromium(III) ecotoxicity to aquatic and terrestrial plants, in *Chromium in Plants and Environment*, ed. N. Kumar, C. Walther and D. K. Gupta, Springer, Cham, 2023, pp. 63–90.

11 Y. Tian, Q. Zhu, J. Yuan, R. Kneepkens, Y. Yue and C. Zhang, *J. Reprod. Dev.*, 2021, **67**, 283–290.

12 K. P. Nickens, S. R. Patierno and S. Ceryak, *Chem.-Biol. Interact.*, 2010, **88**, 276–288.

13 H. Sun, J. Brocato and M. Costa, Oral chromium exposure and toxicity, *Curr. Environ. Health Rep.*, 2015, **2**, 295–303.

14 T. L. DesMarais and M. Costa, *Curr. Opin. Toxicol.*, 2019, **14**, 1–7.

15 V. Singh, N. Singh, M. Verma, R. Kamal, R. Tiwari, M. Sanjay Chivate, S. N. Rai, A. Kumar, A. Singh, M. P. Singh, E. Vamanu and V. Mishra, *Antioxidants*, 2022, **11**, 2375.

16 N. J. Miller Ihli, *J. Food Compos. Anal.*, 1996, **9**, 290–300.

17 K. Oktor, S. Yılmaz, G. Türker and E. Erkuş, *Environ. Monit. Assess.*, 2008, **141**, 97–103.

18 J. J. Thompson and R. S. Houk, *Anal. Chem.*, 1986, **58**, 2541–2548.

19 A. Rajib, I. Saiful, A. Razu, R. Tariqur, R. Atowar and B. I. Abu, *Am. J. Eng. Res.*, 2016, **5**, 243–247.

20 D. C. Prabhakaran, J. Riotte, Y. Sivry and S. Subramanian, *Electroanalysis*, 2017, **29**, 1222–1231.

21 S. Sangsin, P. Dornbundit and P. Tongraung, *Spectrochim. Acta, Part A*, 2021, **246**, 119050.

22 A. J. Weerasinghe, C. Schmiesing and E. Sinn, *Tetrahedron Lett.*, 2009, **50**, 6407–6410.

23 S. Wu, K. Zhang, Y. Wang, D. Mao, X. Liu, J. Yu and L. Wang, *Tetrahedron Lett.*, 2014, **55**, 351–353.

24 D. Xue, C. Zheng, C. Fan, G. Liu and S. Pu, *J. Photochem. Photobiol., A*, 2015, **303–304**, 59–66.

25 H. Zhang, G. Zhang, J. Xu, Y. Wen, S. Ming, J. Zhang and W. Ding, *Spectrochim. Acta, Part A*, 2018, **191**, 79–87.

26 M. Zhang, L. Gong, C. Sun, W. Li, Z. Chang and D. Qi, *Spectrochim. Acta, Part A*, 2019, **214**, 7–13.

27 Y. Zhou, H. Zhao, C. Li, P. He, W. Peng, L. Yuan, L. Zeng and Y. He, *Talanta*, 2012, **97**, 331–335.

28 M. L. Firdaus, I. Fitriani, S. Wyantuti, Y. W. Hartati, R. Khaydarov, J. A. McAlister, H. Obata and T. Gamo, *Anal. Sci.*, 2017, **33**, 831–837.

29 G. S. Ghodake, S. K. Shinde, R. G. Saratale, A. A. Kadam, G. D. Saratale, A. Syed, F. Ameen and D. Y. Kim, *Beilstein J. Nanotechnol.*, 2018, **9**, 1414–1422.

30 W. Wei, Y. Du, L. Zhang, Y. Yang and Y. Gao, *J. Mater. Chem. C*, 2018, **6**, 8793–8803.

31 D. G. Thompson, A. Enright, K. Faulds, W. E. Smith and D. Graham, *Anal. Chem.*, 2008, **80**, 2805–2810.

32 N. E. Motl, A. F. Smith, C. J. DeSantis and S. E. Skrabalak, *Chem. Soc. Rev.*, 2014, **43**, 3823–3834.

33 H. H. Nguyen, J. Park, S. Kang and M. Kim, *Sensors*, 2015, **15**, 10481–10510.

34 E. Petryayeva and U. Krull, *Anal. Chim. Acta*, 2011, **706**, 8–24.

35 S. Jayalakshmi, P. K. Suresh, D. Govindan, M. Mariappan, F. Ameen and A. Veerappan, *Opt. Mater.*, 2024, **154**, 115679.

36 Z. Zhang, Q. Dong, Y. Cao, Y. Liu and Y. Zhao, *Nano*, 2022, **17**, 14.

37 Z. Zhang, H. Li, D. Guo, C. Hu and Y. Liu, *J. Anal. Sci. Technol.*, 2023, **14**, 40.

38 W. Jin, P. Huang, Y. Chen, *et al.*, *J. Nanopart. Res.*, 2015, **17**, 358.

39 M. Elavarasi, A. Rajeshwari, N. Chandrasekaran and A. Mukherjee, *Anal. Methods*, 2013, **5**, 6211–6218.

40 C. Dong, G. Wu, Z. Wang, W. Ren, Y. Zhang, Z. Shen, T. Li and A. Wu, *Dalton Trans.*, 2016, **45**, 8347–8354.

41 H. Yuan, L. Sun, M. Chen and J. Wang, *J. Food Sci.*, 2016, **81**, C1662–C1668.

42 M. A. Toledano-Medina, J. Perez-Aparicio, R. Moreno-Rojas and T. Merinas-Amo, *Food Chem.*, 2016, **199**, 135–139.

43 X. Zhang, N. Li, X. Lu, P. Liu and X. Qiao, *J. Sci. Food Agric.*, 2015, **96**, 2366–2372.

44 S. Kimura, Y. C. Tung, M. H. Pan, N. W. Su, Y. J. Lai and K. C. Cheng, *J. Food Drug Anal.*, 2017, **25**, 62–70.

45 W. C. W. Chang, Y. T. Chen, H. J. Chen, C. W. Hsieh and P. C. Liao, *J. Agric. Food Chem.*, 2020, **68**, 14049–14058.

46 F. Li, J. Cao, Q. Liu, X. Hu, X. Liao and Y. Zhang, *Food Chem.*, 2020, **318**, 126517.

47 M. Iciek, I. Kwiecien and L. Wlodek, *Environ. Mol. Mutagen.*, 2009, **50**, 247–265.

48 P. Z. Trio, S. You, X. He, J. He, K. Sakao and D. X. Hou, *Food Funct.*, 2014, **5**, 833–844.

49 T. Kamoi, *Phosphorus, Sulfur Silicon Relat. Elem.*, 2019, **194**, 698–700.

50 Y. Yamaguchi and H. Kumagai, *Exp. Ther. Med.*, 2019, **19**, 1528–1535.

51 *The Science and Therapeutic Application of Allium Sativum L and Related Species*, H. P. Koch and L. D. Lawson, Williams & Wilkins, Baltimore, Md, USA, 1996.

52 H. Amagase, B. L. Petesch, H. Matsuura, S. Kasuga and Y. Itakura, *J. Nutr.*, 2001, **131**, 955S–962S.

53 H. Amagase, *J. Nutr.*, 2006, **136**, 716S–725S.

54 F. Albrecht, R. Leontiev, C. Jacob and A. J. Slusarenko, *Molecules*, 2017, **22**, 770.

55 T. Fujii, T. Matsutomo and Y. Kodera, *J. Agric. Food Chem.*, 2018, **66**, 10506–10512.

56 R. Paw, M. Hazarika, P. K. Boruah, A. J. Kalita, A. K. Guha, M. R. Das and C. Tamuly, *RSC Adv.*, 2021, **11**, 14700–14709.

57 N. Borah, D. Gogoi, N. C. Ghosh and C. Tamuly, *Food Chem.*, 2023, **15**, 133975.

58 ICH Q2, *Validation of Analytical Procedures: Test and Methodology*, 2005.

59 R. Painuli, S. Raghav and D. Kumar, *ACS Omega*, 2019, **4**, 3635–3645.

60 R. Paw, A. K. Guha and R. Tamuly, *RSC Adv.*, 2024, **14**, 22701–22713.

61 Y. Zhao and D. G. Truhlar, *Theor. Chem. Acc.*, 2008, **120**, 215–241.

62 M. J. Frisch, G. W. Trucks, H. B. Schlegel and G. E. Scuseria, *et al.*, *Gaussian 16, Revision A.03*, Gaussian, Inc., Wallingford CT, 2016.

63 A. E. Reed, L. A. Curtiss and F. Weinhold, *Chem. Rev.*, 1988, **88**, 899–926.

64 D. H. Wi, H. Yang, Y. Kim, H. Ahn, J. W. Hong and S. W. Han, *J. Mater. Chem. A*, 2023, **11**, 1343–1350.

65 L. Q. Lu and Y. Wang, *J. Mater. Chem.*, 2011, **21**, 17916.

66 M. Li, H. Liu, S. Pang, P. Yan, M. Liu, M. Ding and B. Zhang, *Nanomaterials*, 2021, **11**, 2650.

67 G. H. Major, J. W. Pinder, D. E. Austin, D. R. Baer, *et al.*, *J. Vac. Sci. Technol., A*, 2023, **41**, 038501.

68 J. W. Pinder, G. H. Major, D. R. Baer, J. Terry, *et al.*, *Appl. Surf. Sci. Adv.*, 2024, **19**, 100534.

69 S. Ravi, S. Zhang, Y. R. Lee, K. K. Kang, J. M. Kim, J. W. Ahn and W. S. Ahn, *J. Ind. Eng. Chem.*, 2018, **67**, 210–218.

70 J. Zhang, M. Zhang, H. Wan, J. Zhou and A. Lu, *Nat. Commun.*, 2025, **16**, 320.

71 Z. Zhang, X. Ye, Q. Liu, Y. Liu and R. Liu, *J. Anal. Sci. Technol.*, 2020, **11**, 10.

72 F. K. Alqarawi, M. F. Alkahtany, K. H. Almadi, G. A. A. Ben, F. A. Alshahrani, M. H. AlRefeai, I. Farooq, F. Vohra and T. Abduljabbar, *Polymers*, 2021, **13**, 1555.

73 R. Moreno-Tovar, E. Terres and J. R. Rangel-Mendez, *Appl. Surf. Sci.*, 2014, **303**, 373–380.

74 L. Wade and J. Simek, *Organic Chemistry*, 9th edn, Pearson, 2016, p.189.

75 Y. Z. Hamada, N. Bayakly, M. Shafi, S. Painter, V. Taylor, J. Greene and K. Rosli, *Complex Met.*, 2014, **1**, 46–51.

76 A. Imai and E. F. Gloyna, *Water Res.*, 1990, **24**, 1143–1150.

77 M. Liu, H. Zhang, X. Zhang, Y. Deng, W. Liu and H. Zhan, *Water Environ. Res.*, 2001, **73**, 322–328.

78 J. Chwastowska, W. Skwara, E. Sterlinska and L. Pszonicki, *Talanta*, 2005, **66**, 1345–1349.

79 S. Panda, P. B. Pati and S. S. Zade, *Chem. Commun.*, 2011, **47**, 4174–4176.

80 S. I. Hughes, S. S. R. Dasary, A. K. Singh, Z. Glenn, H. Jamison, P. C. Ray and H. Yu, *Sens. Actuators, B*, 2013, **178**, 514–519.

81 S. Bothra, R. Kumar and S. K. Sahoo, *New J. Chem.*, 2017, **41**, 7339–7346.

82 N. Manjubaashini, D. T. Thangadurai, G. Bharathi and D. Nataraj, *J. Lumin.*, 2018, **202**, 282–288.

83 M. L. Firdaus, H. Apriyoanda, I. Isnan, S. Wyantuti and D. R. Eddy, *Iran. J. Chem. Chem. Eng.*, 2023, **42**, 722–730.

84 Y. Q. Dang, H. W. Li, B. Wang, L. Li and Y. Wu, *ACS Appl. Mater. Interfaces*, 2009, **1**, 1533–1538.

85 W. Chen, F. Cao, W. Zheng, Y. Tian, Y. Xianyu, P. Xu, W. Zhang, Z. Wang, K. Deng and X. Jiang, *Nanoscale*, 2015, **7**, 2042–2049.

86 R. P. Modi, V. N. Mehta and S. K. Kailasa, *Sens. Actuators, B*, 2014, **195**, 562–57.